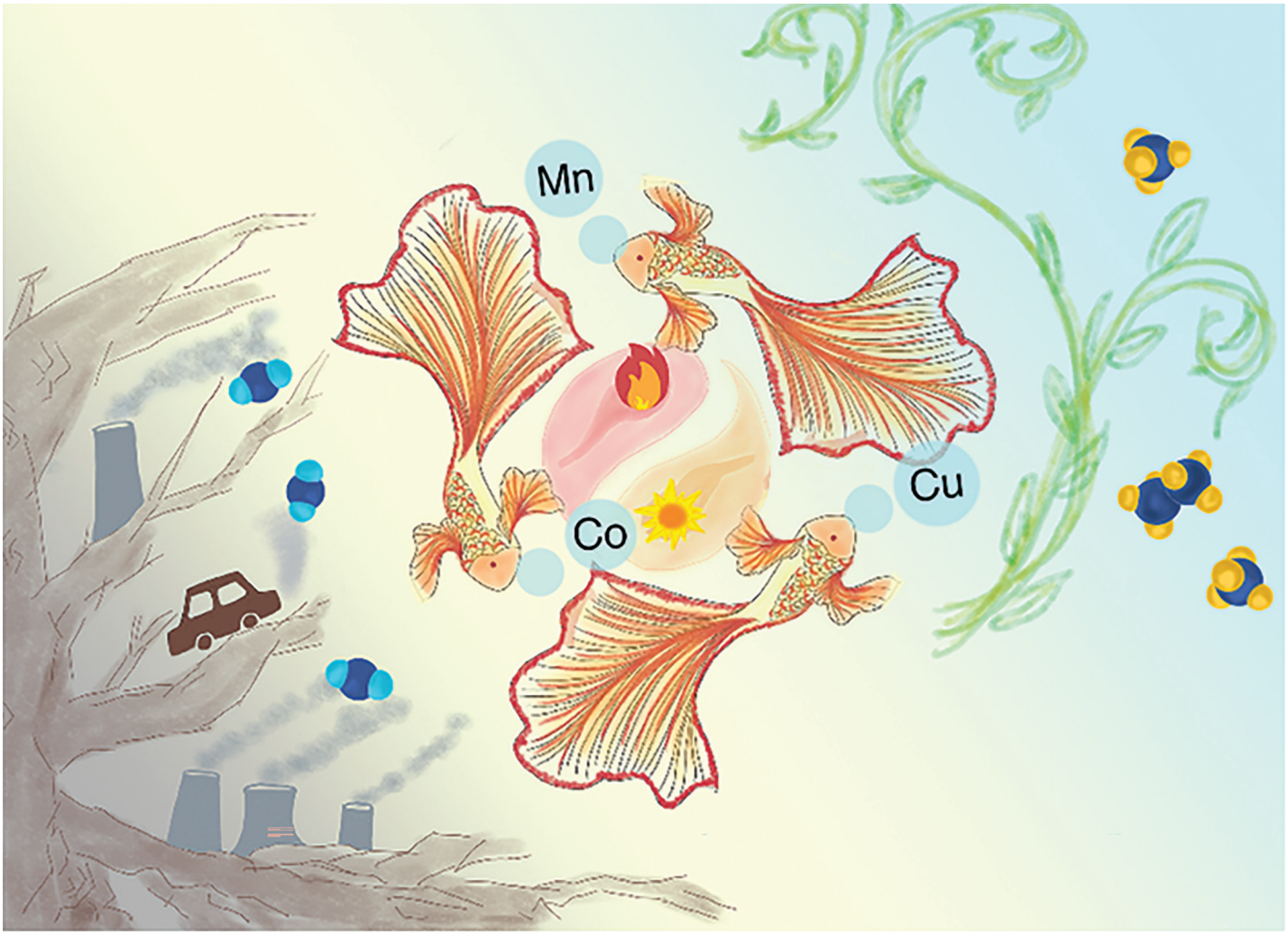

An article presented by Professor Zhen-Hong He and Professor Zhao-Tie Liu from Shaanxi University of Science and Technology and Shaanxi Normal University, China.

Photothermal CO_2 hydrogenation to hydrocarbons over trimetallic Co–Cu–Mn catalysts

Photocatalytic CO_2 reduction is a highly vital process for converting CO_2 into valuable chemicals. However, the reaction always proceeds less efficaciously at low temperature. The combination of photo and thermal conditions is one of feasible approaches to achieve the reaction with high efficiency and has gained much attention recently. In the present work, trimetallic Co–Cu–Mn catalysts were developed in photothermal CO_2 hydrogenation to CH_4 and C_{2+} hydrocarbons. The structural and photoelectric characteristics, as well as adsorption behaviors of these catalysts affected the catalytic performances remarkably.

As featured in:

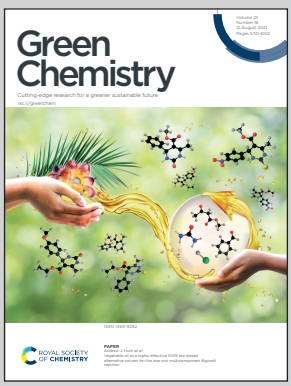

See Zhen-Hong He, Zhao-Tie Liu *et al.*, *Green Chem.*, 2021, **23**, 5775.

ROYAL SOCIETY OF CHEMISTRY

rsc.li/greenchem

Registered charity number: 207890

Green Chemistry

PAPER

View Article Online
View Journal | View Issue

Cite this: *Green Chem.*, 2021, **23**, 5775

Photothermal CO_2 hydrogenation to hydrocarbons over trimetallic Co–Cu–Mn catalysts†

Zhen-Hong He, *[a] Zhu-Hui Li,[a] Zhong-Yu Wang,[a] Kuan Wang,[a] Yong-Chang Sun,[a] Sen-Wang Wang,[b] Wei-Tao Wang,[a] Yang Yang [a] and Zhao-Tie Liu *[a,b]

Photocatalytic CO_2 reduction is a highly vital process for converting CO_2 into valuable chemicals. However, the reaction always proceeds less efficaciously at low temperature. A combination of optical and thermal conditions is one of the feasible approaches to achieve the reaction with high efficiency and has gained much attention recently. In the present work, we prepared several Co–Cu–Mn trimetallic catalysts *via* a simple co-precipitation method, which were used in catalyzing photothermal CO_2 reduction to hydrocarbons. The metal composition and reduction temperature of the catalysts had important effects on their structural and photoelectrical characteristics and adsorption behaviors, further resulting in diverse catalytic performances. Among the prepared trimetallic catalysts, $Co_7Cu_1Mn_1O_x$(200), with a Co/Cu/Mn molar ratio of 7/1/1 and reduced at 200 °C in H_2 for 2 h, could produce CH_4 with an activity of 14.5 mmol g_{cat}^{-1} h^{-1} in 10% CO_2/30% H_2/60% N_2, and CH_4 and C_{2+} hydrocarbons with the activities of 15.9 and 7.5 mmol g_{cat}^{-1} h^{-1} in 25% CO_2/75% H_2, respectively. The present strategy for constructing trimetallic oxide catalysts for the photothermal reaction not only provides a highly active catalyst for CO_2 utilization, but also offers a potential possibility for reducing the high temperature of conventional thermal reactions.

Received 4th April 2021,
Accepted 22nd June 2021

DOI: 10.1039/d1gc01152a

rsc.li/greenchem

Introduction

CO_2 is the primary greenhouse gas, whose concentration in the atmosphere continues to rise.[1] It is also an important C1 source and can be converted into many valuable chemicals such as CO,[2] hydrocarbons,[3–5] olefins,[6] acids,[7–9] alcohols,[10–12] *etc*. Although many efforts have been invested in this area, it is still very difficult to convert CO_2 into chemicals due to its thermodynamic stability and chemical inertness.[1] CO_2 hydrogenation to hydrocarbons represents an essential and green way for its utilization.[13] However, the conventional thermal process is always conducted under harsh conditions, leading to the formation of carbon deposit, the increase of energy consumption, *etc*. The photocatalytic method is an ideal way for the reaction, which could be carried out under mild conditions and using solar energy. However, this route suffers from low activity especially at room temperature, impeding its further applications. Recently, the photothermal catalytic method has gained increasing attention, especially in CO_2 reduction.[14,15]

The photothermal routes always contain four types, including thermal-assisted photocatalysis, photo-assisted thermocatalysis, photothermal co-catalysis, and photo-driven thermocatalysis.[16] Generally, these routes combine the advantages of both photocatalysis and thermal catalysis including high activity, proceeding under mild conditions, efficient energy utilization, *etc*. To date, many catalysts such as Ru/silicon nanowire,[17] $RuO_2/SrTiO_3$,[18] RuO_2/3D silicon photonic crystals,[19] Ru@FL-LDHs (Ru/Mg–Al LDHs matrix),[20] Ru/Al_2O_3,[21] Ru/TiO_2,[22] $Pd@Nb_2O_5$,[23] CoFeAl-LDH nanosheet,[13] $Ni/SiO_2{\cdot}Al_2O_3$,[14] Cu_2O/Zn-MOF,[24] Cu_2O/graphene,[25] *etc*. have been used for photothermal CO_2 hydrogenation, and their catalytic performances are given in Table S1.† Significant advances have been made in recent years; however, most of the above catalysts suffer from drawbacks such as using expensive noble metals, working at high temperature, and exhibiting low activity. Besides, the obtained products mainly focused on C1 chemicals such as CO and CH_4. The synthesis of C_{2+} products *via* a photothermal route is a more difficult but significant issue, which is rarely involved in the above developed catalytic systems.[26] Considering the above aspects, to develop a cost-efficient, highly active and reusable catalyst for photothermal

[a]*Shaanxi Key Laboratory of Chemical Additives for Industry, College of Chemistry and Chemical Engineering, Shaanxi University of Science & Technology, 710021 Xi'an, China. E-mail: hezhenhong@sust.edu.cn, ztliu@snnu.edu.cn*
[b]*School of Chemistry & Chemical Engineering, Shaanxi Normal University, 710119 Xi'an, China*

†Electronic supplementary information (ESI) available. See DOI: 10.1039/d1gc01152a

CO_2 reduction into CH_4 and C_{2+} hydrocarbons is particularly important.

On the other hand, it has been well known that pure metals used in CO_2 hydrogenation always showed a low activity due to their low CO_2 binding capacity.[27] Oxides could not only anchor metal atoms but also provide vacancies for the reaction, and in this way, they could participate in the reaction and enhance the catalytic performances.[28] Trimetallic oxide catalysts show unique electronic and structural features different from their individual components. The complex composition of trimetallic catalysts could form multiple interfaces conducive to catalysis.[29] In this aspect, trimetallic catalysts have been widely used in many reactions such as CO and CO_2 hydrogenation,[30–32] ethanol steam reforming,[33] ammonia oxidation,[34] *etc.* with good performances. In particular, complicated metal–trimetallic oxides can provide many vacancies and active sites for catalysis, and have great potential for application in CO_2 reduction. Herein, a series of Co–Cu–Mn trimetallic oxides were prepared and used for photothermal CO_2 reduction, and the screened $Co_7Cu_1Mn_1O_x(200)$ catalyst, with a Co/Cu/Mn ratio of 7/1/1 and reduced at 200 °C in H_2, showed a high CH_4 formation activity (14.5 mmol g_{cat}^{-1} h^{-1}) even at low CO_2 (10%) and H_2 (30%) concentrations, which lies in the highest activity range in Table S1.† Interestingly, after increasing the CO_2 and H_2 concentrations to 25% and 75%, 15.9 and 7.5 mmol g_{cat}^{-1} h^{-1} of CH_4 and C_{2+} hydrocarbons were produced with selectivities of 65.4% and 30.8%, respectively. Moreover, the catalyst has a good temporal stability under continuous-flow conditions. The metal/oxides were confirmed to be very important for the catalytic performance, in which the Co^0 species were the active sites, which together with the oxides acted as supports and semiconductors for providing a local heating environment *via* the photothermal effects. The Cu species could promote the reduction of Co and Mn oxides, and also promote the coupling of C–C bonds to produce C_{2+} products especially at a high CO_2 concentration. The Mn species could on one hand enhance the adsorption of CO_2 and H_2, and also provide the photothermal effect to produce a local heating effect to promote the reaction. The present strategy for constructing trimetallic catalysts for the photothermal reaction does not only provide a simple but efficient way to convert CO_2 into valuable hydrocarbons, but also offer a general method for reducing the reaction temperature of conventional high-temperature reactions.

Results and discussion

Preparation and characterization of catalysts

Trimetallic Co–Cu–Mn catalysts were prepared by a simple co-precipitation method, and the details are given in the ESI.† The prepared catalysts were denoted as $Co_aCu_bMn_cO_x(T)$, in which $a/b/c$ and T represent the Co/Cu/Mn molar ratio and the reduction temperature, respectively. $Co_aCu_bMn_cO_x$ means unreduced catalysts. The morphologies of the catalysts were examined by TEM tests. Initially, the $Co_7Cu_1Mn_1O_x$ catalyst mainly showed the morphology of nanoparticles with the size range of 6–15 nm (Fig. 1a and b). The lattice spacings of 0.186, 0.246, 0.219, 0.152, 0.197, and 0.135 nm in the HRTEM image

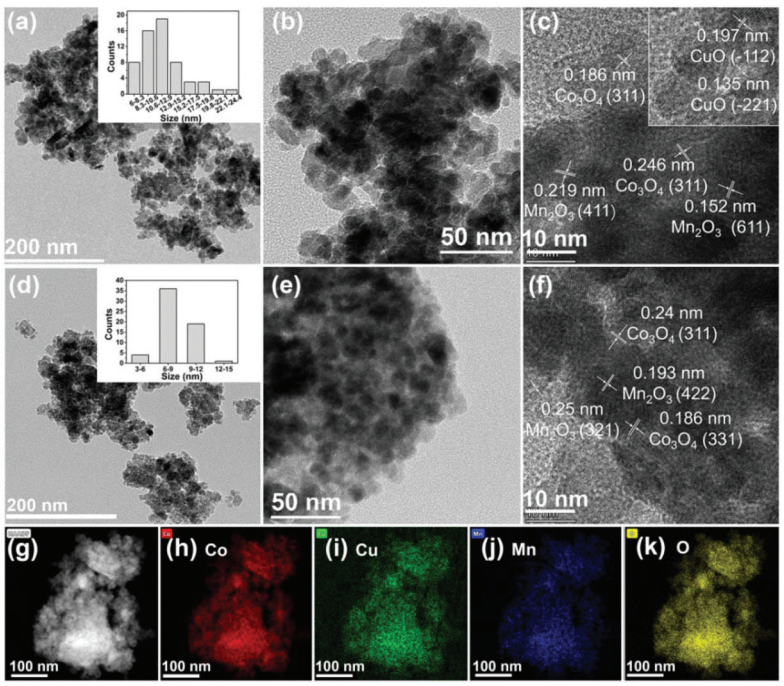

Fig. 1 TEM images (a, b, d, and e) and HRTEM images (c and f) for the $Co_7Cu_1Mn_1O_x$ (a–c) and $Co_7Cu_1Mn_1O_x(200)$ (d–f) catalysts, HAADF-STEM image for the $Co_7Cu_1Mn_1O_x(200)$ catalyst (g) and the corresponding EDS elemental mapping of Co, Cu, Mn, and O (h–k). The insets in (a) and (d) are the size distribution histograms for the $Co_7Cu_1Mn_1O_x$ and $Co_7Cu_1Mn_1O_x(200)$ catalysts.

could be successively indexed to the (331) and (311) planes of Co_3O_4, the (411) and (611) planes of Mn_2O_3, and the (−112) and (−221) planes of CuO (Fig. 1c).

After reduction, the $Co_7Cu_1Mn_1O_x$(200) catalyst maintained the nanoparticle morphology in the size range of 6–12 nm (Fig. 1d and e). Co_3O_4 and Mn_2O_3 were also detected, as shown in Fig. 1f. The HAADF-STEM and EDX elemental mappings of the $Co_7Cu_1Mn_1O_x$(200) catalyst showed that Co, Cu, Mn, and O elements are homogeneously dispersed over the whole grain (Fig. 1g to k).

For comparison, the TEM images of catalysts with different Co/Cu/Mn ratios were also studied, and the results are shown in Fig. S1.† With the increasing Co content, the morphology changed from nanosheets to nanoparticles. For example, the $Co_3Cu_1Mn_1O_x$(200) and $Co_5Cu_1Mn_1O_x$(200) catalysts were nanosheets, while the $Co_7Cu_1Mn_1O_x$(200) and $Co_9Cu_1Mn_1O_x$(200) catalysts were mainly nanoparticles, which were beneficial for exposing more active sites.

The molar ratios of the bimetallic and trimetallic catalysts were tested by ICP-OES, and the results are given in Table S2.† The molar ratios of metals were consistent with the feed amounts.

XRD examinations showed that all the tested unreduced catalysts such as $Co_7Cu_1Mn_1O_x$, $Co_7Mn_1O_x$, and $Co_7Cu_1O_x$ showed the XRD patterns of Co_3O_4 (JCPDS file no. 73-1701). No obvious CuO_x or MnO_x peaks were found, implying that they were easily incorporated into the Co_3O_4 crystals and were well dispersed (Fig. 2a). The $Co_7Cu_1Mn_1O_x$(200) catalyst showed the same peaks as that of the $Co_7Cu_1Mn_1O_x$ catalyst, but with lower intensities, indicating the crystallinity decrease of the Co_3O_4 component after reduction.

The XRD pattern of the $Co_7Cu_1Mn_1O_x$(200) catalyst was almost the same as that of the unreduced catalyst, and it is mainly attributed to the Co_3O_4 phase (Fig. 2b). However, two small peaks at 43.0° and 61.8° were carefully detected, which could be assigned to the CoO (200) and (220) planes (JCPDS file no. 70-2855). No Co^0, Cu^0, Cu_2O, or Mn_2O_3 species were detected due to their low amounts. The $Co_7Mn_1O_x$(200) catalyst showed three peaks at 36.8°, 42.7°, and 61.8°, which could be assigned to the CoO (111), (200), and (220) planes (JCPDS file no. 78-0431), respectively. Two phases of Co^0 fcc and hcp were identified in the $Co_7Cu_1O_x$(200) catalyst, and the formation of two phases is commonly observed in the synthesis of cobalt nanostructures.[35] The peaks at 41.5°, 44.4°, 47.4°, and 75.9° could be indexed to Co^0 hcp (100), (002), (101), and (110) facets (JCPDS file no. 01-071-4239), respectively. The peaks at 44.4° and 51.5° could be contributed to the Co^0 fcc (111) and (200) planes (JCPDS file no. 01-071-4651).[35] The results indicated that Co_3O_4 could be reduced to Co^0 by the promotion of Cu species, and this will be further verified by the following H_2-TPR tests. No MnO_x or CuO_x species were detected due to their good dispersion. It is worth noting that although Cu could promote the reduction of CoO_x species to Co^0, no Co^0 was detected in the bulk phase of the $Co_7Cu_1Mn_1O_x$(200) catalyst.

The XRD patterns of the catalysts with different Co/Cu/Mn ratios also showed the main peaks of Co_3O_4 and CoO (Fig. S2†); however, the $Co_3Cu_1Mn_1O_x$(200) and $Co_5Cu_1Mn_1O_x$(200) catalysts showed a wide peak at around 20°, indicating that they possess amorphous structures.

The results of the N_2 adsorption/desorption tests are shown in Fig. S3 and Table S3.† The reduction temperature affects the catalyst structure remarkably, and the BET surface areas of the tested trimetallic catalysts declined gradually with the increase of the reduction temperature, which is probably because the high reduction temperature leads to catalyst sintering. The bimetallic Co–Cu catalyst shows the lowest BET surface area, while the Co–Mn catalyst presents the highest. Indeed, the surface areas of the CoO_x and $Co_7Cu_1Mn_1O_x$(100, 200, and 300) catalysts did not differ greatly from one another, thus their diverse performances did not stem from the difference in their surface areas.

To distinguish the valences of the Co, Cu, and Mn species on the surface of the catalysts, the XPS of Co 2p, Cu 2p, Mn 2p and 3s, and AES of Cu $L_3M_{4,5}M_{4,5}$ were analyzed (Fig. 3).[5,36,37] In the XPS of the $Co_7Cu_1Mn_1O_x$ catalyst, the Co element was composed of Co^{3+} and Co^{2+} species, which was confirmed by the peaks at 779.5 eV and 780.9 eV, which can be attributed to the Co^{3+} and Co^{2+} $2p_{3/2}$ peaks (Fig. 3a).[38] The Cu^{2+} 2p XPS showed two peaks at 934.5 eV and 954.2 eV, which could be assigned to Cu^{2+} $2p_{3/2}$ and $2p_{1/2}$, respectively (Fig. 3b and c). The XPS peaks of Co species in the $Co_7Cu_1Mn_1O_x$(200) catalyst were the same as those in the unreduced catalyst; however, the Cu species was found to be Cu^+. The Mn XPS indicated that the catalyst contains Mn^{3+} oxidation state (Fig. 3d and e). The XPS results indicated that the surface of the $Co_7Cu_1Mn_1O_x$(200) catalyst mainly contained Co^{2+}, Co^{3+}, Cu^+, a small amount of Cu^{2+}, and Mn^{3+}, respectively, but no Co^0 or Cu^0 species were detected for air oxidation.

For comparison, the XPS spectra of the catalysts reduced at different temperatures were also tested. The Co element in these catalysts was mainly composed of Co^{2+} and Co^{3+} species

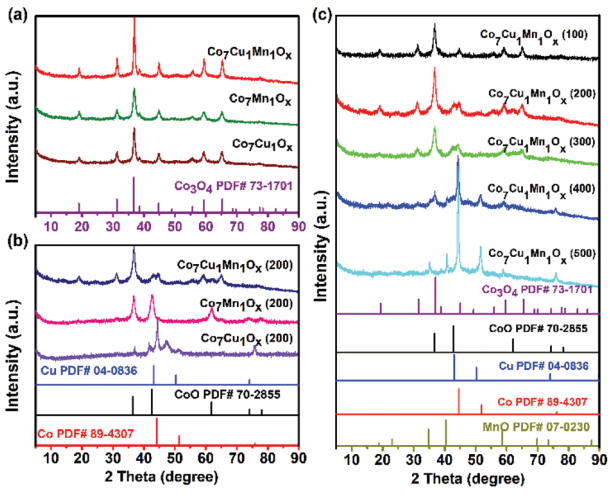

Fig. 2 XRD patterns of (a) the unreduced $Co_7Mn_1O_x$, $Co_7Cu_1O_x$, and $Co_7Cu_1Mn_1O_x$ catalysts; (b) $Co_7Mn_1O_x$(200), $Co_7Cu_1O_x$(200), and $Co_7Cu_1Mn_1O_x$(200); and (c) $Co_7Cu_1Mn_1O_x$ catalysts reduced at different temperatures.

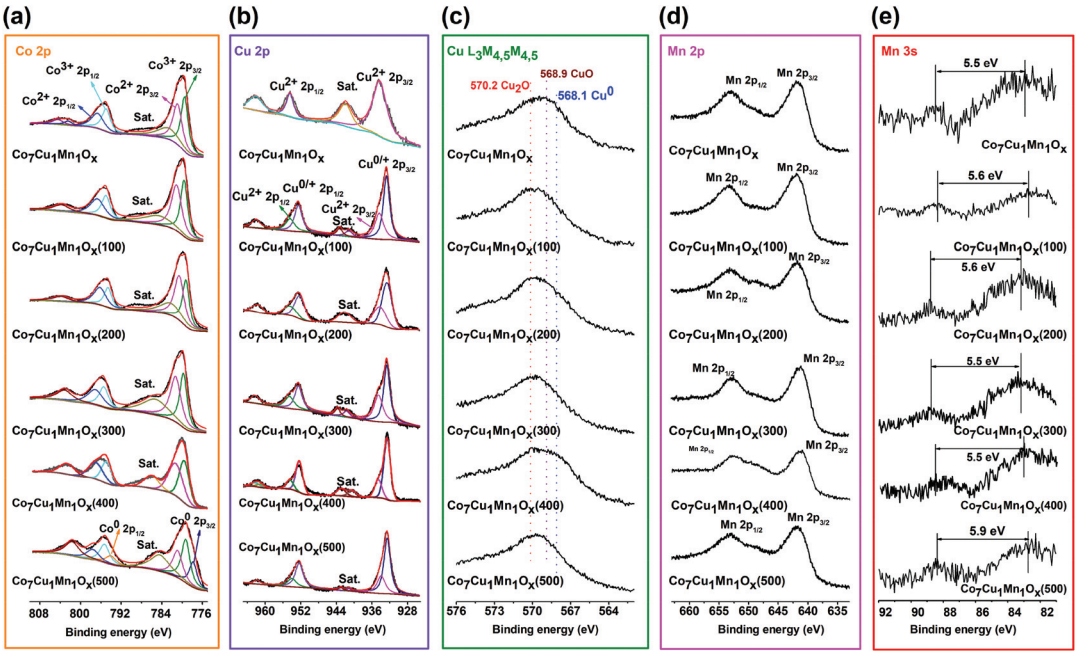

Fig. 3 XPS spectra of the unreduced $Co_7Cu_1Mn_1O_x$ catalyst and the $Co_7Cu_1Mn_1O_x$(100, 200, 300, and 500) catalysts. (a) Co 2p XPS, (b) Cu 2p XPS, (c) Cu $L_3M_{4,5}M_{4,5}$ AES spectra, (d) Mn 2p XPS, and (e) Mn 3s XPS, respectively.

but with different contents. The Co^{2+} component increased with the increase of the reduction temperature. No obvious Co^0 species was found until the reduction temperature reached 500 °C. As for the Cu XPS, the area of the satellite peak around 942 eV decreased with increasing reduction temperature, indicating that $Cu^{0/+}$ $2p_{3/2}$ increased. Besides, all the reduced catalysts possess the dominant Cu^+ component. The Mn 3s XPS showed that the $Co_7Cu_1Mn_1O_x$(500) catalyst is composed of Mn^{2+} species, *i.e.*, MnO, while the others showed Mn^{3+} species.

The XPS spectra of the Co–Cu–Mn trimetallic catalysts with different molar ratios were also investigated, and the results are given in Fig. S4.† All the elements had the same valences but contained different contents, such as Co^{2+}, Co^{3+}, Mn^{3+}, Cu^+, and a small amount of Cu^{2+}, which are similar to the $Co_7Cu_1Mn_1O_x$(200) catalyst, indicating that they are probably active in the reaction. This was confirmed by the following catalytic activity studies (Table 1).

The Raman spectrum of the $Co_7Cu_1Mn_1O_x$(200) catalyst showed a peak at 680 cm^{-1}, which could be assigned to the A1 g mode of Co_3O_4 (Fig. S5†).[39] This profile is similar to those of the $Co_7Cu_1Mn_1O_x$ and $Co_7Cu_1Mn_1O_x$ (100, 300, and 400) catalysts, indicating that Co_3O_4 exists in these catalysts. Interestingly, the $Co_7Cu_1Mn_1O_x$(500) catalyst showed a wide peak at 540 cm^{-1}, assigned to the one-phonon LO mode of CoO,[40] which was formed by the partial oxidation of Co^0 by local laser heating.[45] No obvious Cu or Mn species were detected, indicating that they have permeated into the Co_3O_4 crystal lattice.

The above characterization studies showed that the $Co_7Cu_1Mn_1O_x$(200) catalyst mainly possesses Co_3O_4 in the bulk phase, while the surface of the catalyst was composed of Co^{3+}, Co^{2+}, Mn^{3+}, Cu^+, and a small amount of Cu^{2+} species, which are in the forms of Co_3O_4, Mn_2O_3, Cu_2O, and CuO. The catalysts reduced at 100, 200, and 300 °C, and the catalysts with different Co/Cu/Mn molar ratios contained similar components but of different concentrations, indicating that they possess similar structures and properties.

Catalytic performances

Photothermal CO_2 hydrogenation was carried out in a tubular reactor (Fig. S6),† and the procedure details are given in the ESI.† The products of photothermal CO_2 reduction include CO, CH_4, and C_{2+} hydrocarbons (mainly C_2 to C_6) in the present work. Initially, the catalytic performances over different catalysts are given in Table 1. No products were detected in the absence of a catalyst, and the sole metal catalysts or the bimetallic catalysts showed a very low activity in the reaction. The $Co_7Cu_1Mn_1O_x$(200) catalyst showed the best catalytic performances with a CH_4 formation activity of 14.5 mmol g_{cat}^{-1} h^{-1} and a selectivity of 85.3% (entries 1–7 *vs.* 8). These activities were achieved under the irradiation of a 300 W Xe lamp (234 mW cm^{-2}, 300–1100 nm) and heat generated by an additional electric heater (Fig. S6†). Unlike the CuO_x(200) and MnO_x(200) catalysts, the CoO_x(200) catalyst could show a very low CH_4 formation activity (only 3.1 mmol g_{cat}^{-1} h^{-1}) (entries 2–4), demonstrating that the Co species is probably the active species, while the CuO_x and MnO_x species are the promoters for the Co species. Indeed, the Cu and Mn species are always used as promoters or active sites for the Co-catalyzed CO_2 reduction.[41] The activities of the bimetallic $Cu_1Mn_1O_x$ or $Co_7Mn_1O_x$ catalysts confirmed that Cu or Mn are not the active sites (entries 5–7). Interestingly, the $Co_7Cu_1O_x$(200) catalyst showed higher activities for the formation of CH_4 and C_{2+}

Table 1 Photothermal CO_2 hydrogenation over diverse catalysts[a]

Entry	Catalyst	Conv. (%)	Activity[b] (mmol g_{cat}^{-1} h^{-1})			CH_4[b] Sele. (%)
			CH_4	C_{2+}	CO	
1	None	0	0	0	0	—
2	CoO_x(200)	5.6	3.1 ± 0.1	0.4 ± 0.1	0	88.6
3	CuO_x(200)	0	0	0	0	—
4	MnO_x(200)	0	0	0	0	—
5	$Cu_1Mn_1O_x$(200)	0	0	0	0	—
6	$Co_7Mn_1O_x$(200)	0.8	0.2 ± 0.1	0	0.3 ± 0.1	40.0
7	$Co_7Cu_1O_x$(200)	14.0	5.9 ± 0.2	2.4 ± 0.1	0.4 ± 0.1	67.8
8	$Co_7Cu_1Mn_1O_x$(200)	27.4	14.5 ± 0.2	1.4 ± 0.1	1.1 ± 0.1	85.3
9	$Co_3Cu_1Mn_1O_x$(200)	12.4	7.2 ± 0.2	0.5 ± 0.2	0	93.5
10	$Co_5Cu_1Mn_1O_x$(200)	16.8	9.4 ± 0.3	0.8 ± 0.2	0.2 ± 0.2	84.7
11	$Co_9Cu_1Mn_1O_x$(200)	18.9	10.1 ± 0.2	0.9 ± 0.2	0.7 ± 0.1	90.4
12	$Co_1Cu_3Mn_1O_x$(200)	3.1	1.6 ± 0.2	0.3 ± 0.1	0	84.2
13	$Co_1Cu_1Mn_3O_x$(200)	2.1	1.1 ± 0.2	0.2 ± 0.1	0	84.6
14[c]	$Co_7Cu_1Mn_1O_x$(200)	28.4	15.1 ± 0.2	1.3 ± 0.1	1.2 ± 0.1	85.8
15	$Co_7Cu_{0.25}Mn_{1.75}O_x$(200)	13.6	7.7 ± 0.1	0.4 ± 0.2	0.4 ± 0.1	90.6
16	$Co_7Cu_{0.75}Mn_{1.25}O_x$(200)	22.9	12.7 ± 0.2	0.7 ± 0.1	0.9 ± 0.1	88.8
17	$Co_7Cu_{1.25}Mn_{0.75}O_x$(200)	24.0	11.5 ± 0.2	2.6 ± 0.1	0.9 ± 0.1	76.7
18	$Co_7Cu_{1.75}Mn_{0.25}O_x$(200)	14.1	5.0 ± 0.1	2.5 ± 0.1	1.3 ± 0.1	56.8

[a] Reaction conditions: catalyst 50 mg, $CO_2/H_2/N_2$ 10%/30%/60%, full irradiation, 200 °C, 3 h. [b] Detected by GC and obtained from three successive runs. [c] N_2 was replaced by Ar.

hydrocarbons than those of the pure CoO_x(200) and CuO_x(200) catalysts, indicating that the Cu species could not only enhance the activity of the Co-based catalyst in CO_2 reduction to CH_4, but also promote the formation of C_{2+} products. For comparison, other trimetallic catalysts with different ratios were also assessed; however, all of them possessed lower activities than that of the $Co_7Cu_1Mn_1O_x$(200) catalyst (entries 8 *vs.* 9–13).

The activities achieved in $CO_2/H_2/N_2$ and CO_2/H_2/Ar were very similar (entries 8 *vs.* 14), indicating that the catalytic performances were not affected by the type of diluent gas. In addition, the C_{2+} activities of the $Co_9Cu_1Mn_1O_x$(200), $Co_7Cu_1Mn_1O_x$(200), $Co_5Cu_1Mn_1O_x$(200), and $Co_3Cu_1Mn_1O_x$(200) catalysts were only 0.9, 1.4, 0.8, and 0.5 mmol g_{cat}^{-1} h^{-1}, respectively, and inconsistent with the change rule of the catalyst composition. Because the formation of C_{2+} products is closely related to the Cu species, the uneven distribution of Cu species on the catalyst surface is probably the reason for the discrepancy between the C_{2+} activity and the Co/Cu/Mn molar ratio of the catalyst.

The Co species are the active sites; however, the promoters of Cu and Mn species are also very important for the reaction. To confirm this, the catalysts with the same component of Co element were investigated, and the results indicated that the Cu and Mn concentrations affected the catalytic performances remarkably (entries 15–18). The $Co_7Cu_{0.75}Mn_{1.25}O_x$(200) and $Co_7Cu_{1.25}Mn_{0.75}O_x$(200) catalysts showed high CH_4 formation activities, while the $Co_7Cu_{0.25}Mn_{1.75}O_x$(200) and $Co_7Cu_{1.75}Mn_{0.25}O_x$(200) catalysts offered relatively low values, indicating that the low concentrations of Cu and Mn are not beneficial for catalysis.

The catalytic performance studies showed that the coexistence of Co, Cu, and Mn in the Co/Cu/Mn trimetal is very important for the reaction, and their molar ratios and the synergistic effects of these multicomponents are closely related to the catalytic performances, and a similar phenomenon could be found in the previous report.[42]

Effect of the reduction temperature of the $Co_7Cu_1Mn_1O_x$ catalysts

The above characterization results indicated that the reduction temperature affected the metal valence compositions of the catalysts, and it was proved to be able to affect their catalytic performances.[43,44] To verify this, the catalysts reduced at different temperatures were studied, and the results are shown in Fig. 4. Indeed, the $Co_7Cu_1Mn_1O_x$ and $Co_7Cu_1Mn_1O_x$(100, 200, and 300) catalysts showed good catalytic performances during the reaction, indicating that they have similar catalyst

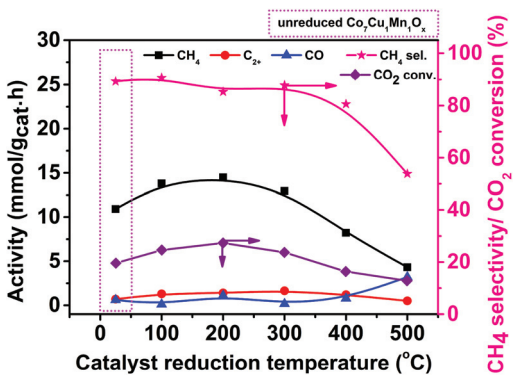

Fig. 4 Effect of the reduction temperature of the $Co_7Cu_1Mn_1O_x(T)$ catalysts on the catalytic performances of photothermal CO_2 reduction. Reaction conditions: catalyst 50 mg, $CO_2/H_2/N_2$ 10%/30%/60%, 200 °C, 3 h, and 300 W Xe lamp full irradiation.

compositions and properties. However, the $Co_7Cu_1Mn_1O_x$(400 and 500) catalysts showed decreased catalytic activities, which has a great relationship with the high concentration of Co^0 in the bulk phase but less Co_3O_4 and Mn_2O_3.

The catalysts after being used for 9 h and 21 h were characterized by XPS and XRD in Fig. 5, and the results showed that Co^0 and Cu^0 species could be found during the reaction. Co^0 was widely recognized as the active site for CO_2 hydrogenation. The XRD patterns of the catalysts used for 9 h showed similar peaks to those of Co_3O_4 and CoO, revealing that Co_3O_4 still exists in the bulk phase. Compared with the $Co_7Cu_1Mn_1O_x$(200) catalyst in Fig. 2, the peak at 36.6° decreased remarkably. The catalyst used for 21 h showed similar results but with more Co^0 and Cu^0 species. The XPS and XRD characterization studies showed that the catalyst compositions were stable during the reaction.

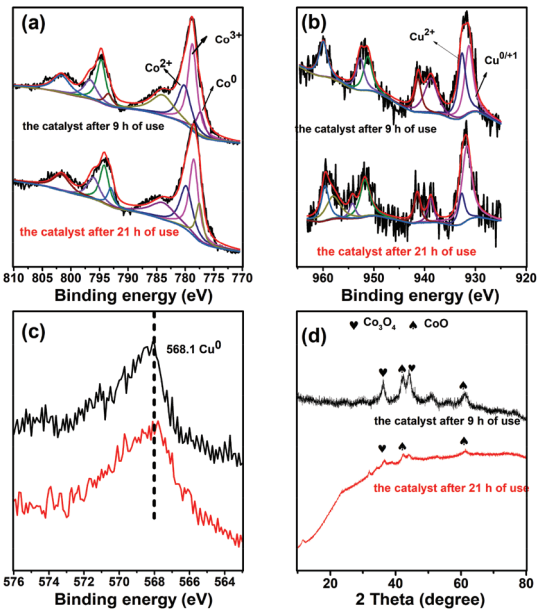

Fig. 5 XPS tests (a, Co 2p; b, Cu 2p; c, Cu 3s LMM AES) and XRD pattern (d) for the catalysts after 9 h and 21 h of uses, respectively.

The highest CH_4 activity was achieved over the $Co_7Cu_1Mn_1O_x$(200) catalyst. Besides, the $Co_7Cu_1Mn_1O_x$(100 and 300) catalysts also showed acceptable CH_4 formation activities. Generally, in thermal catalysis, Co^0 species are recognized as the active components. However, the $Co_7Cu_1Mn_1O_x$(500) catalyst showed the lowest activity in the reaction, which mainly contained the Co^0 species but no Co_3O_4 or Mn_2O_3. It should be noted that in the present photothermal catalysis, the oxides including Co_3O_4, Mn_2O_3, *etc.* could promote the reaction *via* the interaction effect between the Co species and other oxides.

The H_2-TPR tests were carried out to study the interaction effect of different metal oxides, and the results are shown in Fig. 6. Pure Co_3O_4 showed two peaks at 273 °C and 336 °C, which could be assigned to the reduction peaks of Co_3O_4 to CoO and CoO to Co^0, respectively.[46] Mn_2O_3 showed two peaks located at 292 °C and 388 °C, which could be assigned to the reduction of Mn_2O_3 to Mn_3O_4 and Mn_3O_4 to MnO, respectively.[47,48] The $Co_7Cu_1O_x$ catalyst had two peaks at lower temperatures of 156 °C and 210 °C indicating that Cu could obviously promote the reduction of Co_3O_4 and CoO, which is consistent with previous reports.[45] However, the $Co_7Mn_1O_x$ catalyst showed two main peaks at 280 °C and 428 °C, which could be assigned to the reduction of $(Co,Mn)_3O_4$ to (Co,Mn)O, and (Co,Mn)O to Co^0 and MnO,[5,49,50] respectively, revealing that Mn species impedes the reduction of CoO_x. The $Co_7Cu_1Mn_1O_x$ catalyst had three peaks at 128, 183, and 284 °C, which could be attributed to the reduction peaks of CuO to Cu^0, Co_3O_4 to CoO, and CoO to Co^0 and MnO, respectively.[50] The H_2-TPR results indicated that the Co, Cu, and Mn species show strong interaction effects, and the previous report showed that the presence of Cu could alter the electronic interactions with Co and Ni in the Co–Cu–Ni trimetallic catalysts.[30]

The surface adsorption capacities could significantly affect the catalytic activity. Thus, we conducted the CO_2-TPD and H_2-TPD tests for the diverse trimetallic catalysts and the results indicated that with the increase of the reduction temperature, the adsorption amounts of CO_2 and H_2 on the catalysts decreased. The $Co_7Cu_1Mn_1O_x$(100 and 200) catalysts contained higher CO_2 and H_2 adsorption amounts than the others,

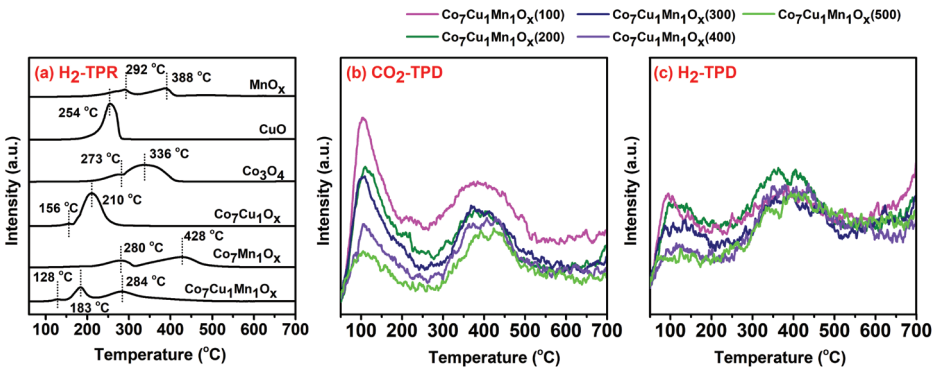

Fig. 6 H_2-TPR(a), CO_2-TPD (b), and H_2-TPD (c) tests for the different catalysts.

which is beneficial for them to catalyze the CO_2 photothermal reduction.

To investigate the effects of the Mn and Cu species on the Co-based catalysts, the CO_2-TPD tests for Co–Mn and Co–Cu bimetallic catalysts were performed (Fig. S7†). The Mn species was found to be able to improve CO_2 and H_2 adsorption for the Co-based catalysts, while the Cu species reduced their adsorption since the Co–Cu bimetallic catalyst could be deeply reduced at 200 °C. Even so, the $Co_7Cu_1O_x(200)$ catalyst exhibited a strong CO_2 adsorption peak at around 350 °C, showing that the Cu species could promote strong adsorption of CO_2 on the catalyst.

We investigated the catalytic performances of the Co–Cu and Co–Mn bimetallic catalysts reduced at different temperatures, and the results are given in Table S4.† With the increase of the reduction temperature, the activities of the Co–Cu and Co–Mn catalysts increased initially but were then reduced at high reduction temperatures of 400 and/or 500 °C. The highest activities were lower than that of the $Co_7Cu_1Mn_1O_x(200)$ catalyst (Table 1, entry 8), indicating that the Cu and Mn species were both needed for the photothermal CO_2 reduction.

Effect of the reaction conditions

The above investigation showed the composition and pretreatment of the catalyst affected the activity remarkably. In addition, the reaction conditions also had a great influence on the catalytic performance. The effects of the reaction conditions on the catalytic performance were also investigated, and the results are shown in Fig. 7. Almost no product was detected in the absence of CO_2 or H_2, indicating that the products are generated from CO_2. This was further confirmed by a control experiment of adding $^{13}CO_2$ in the reaction, in which $^{13}CH_4$ was detected with a mass spectrometer (Fig. S8†).

The best performances for CH_4 formation were achieved in CO_2/H_2 with a molar ratio of 1/3 (Fig. 6a). Surprisingly, changing the CO_2 and H_2 concentrations slightly affected the activity of CH_4 formation (around 15 mmol g_{cat}^{-1} h^{-1}), but had an influence on C_{2+} hydrocarbon formation. In the absence of a dilute gas, the highest C_{2+} activity reached 7.5 mmol g_{cat}^{-1} h^{-1} with a 30.8% selectivity. Generally, C_{2+} hydrocarbon formation involves CO_2 reduction and C–C coupling steps, and is much more difficult to achieve under photothermal conditions.[51] Thus, the present $Cu_7Cu_1Mn_1O_x(200)$ catalyst could catalyze the C_{2+} hydrocarbon formation, but only the CO_2 and H_2 concentrations need to be enhanced. The C_{2+} formation is strongly linked to the amount of surface adsorbed carbon species such as CO, $-CH_2-$, *etc.* A high amount of carbon species can be coupled to generate C_{2+} hydrocarbons over a suitable catalyst, thus an increase of the CO_2 concentration could enhance the C_{2+} selectivity. However, generally, to obtain C_{2+} products, high pressure and/or CO_2/H_2 molar ratio are always needed.[42] The present $Co_7Cu_1Mn_1O_x(200)$ catalyst has a good CO_2 adsorption capacity, which was confirmed by the CO_2-TPD tests. The high C_{2+} selectivity indicates that the $Co_7Cu_1Mn_1O_x(200)$ catalyst possesses good CO_2 reduction and C–C coupling abilities even under ambient pressure and a low CO_2/H_2 molar ratio (1/3). These multi-functional applications of synthesis of CH_4 and C_{2+} hydrocarbons stemmed from the multiple interfaces created by the complicated compositions of Co^0, Co_3O_4, Mn_2O_3, CuO and Cu_2O species, *etc.*

The reaction temperature has a significant influence on the catalytic performance, which was monitored using a thermocouple positioned above the catalyst level (Fig. S6†). As shown in Fig. 7c, high temperature promoted the reaction remarkably. With the increase of the reaction temperature, the activity of CH_4 formation increased. The C_{2+} selectivity increased initially and then slightly decreased at a temperature higher than 200 °C. This is probably because at high temperature, the catalyst was sintered and reduced, which affected the product distribution especially with the CH_4 selectivity increased and C_{2+} products decreased.

The evolution of activity on reaction time was also studied and the results are shown in Fig. 7d. In the first 30 min of reaction, CH_4 was formed with a very low activity, indicating that the catalyst had an induction period. During this period, the surface Co species, especially the surface CoO was reduced to the active Co^0 species. With prolonged time, the CH_4 formation activity increased remarkably. During our experiments, we found that the pressure of the reaction gas decreased remarkably after 3 h, but further prolonging the time did not show any remarkable decrease, indicating that the reaction has reached equilibrium. Thus, we chose 3 h as the optimum reaction time. In addition, control experiments were conducted to investigate the effect of optical and thermal conditions. The reaction could hardly occur under light irradiation but without extra heating, and the sole thermal conditions offered a very low CH_4 formation activity (only one-sixth that of

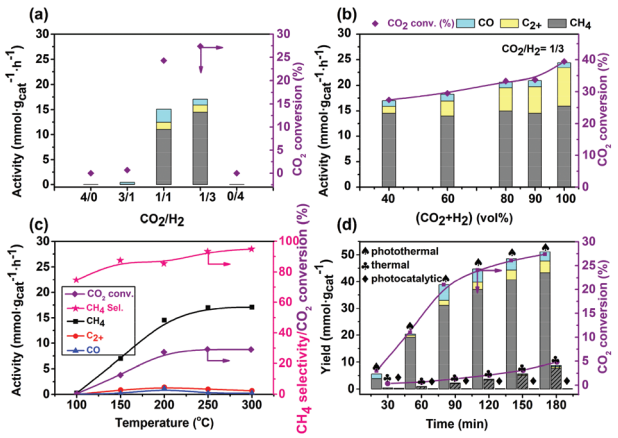

Fig. 7 Effects of the reaction conditions on the catalytic performances of photothermal CO_2 reduction over the $Co_7Cu_1Mn_1O_x(200)$ catalyst; (a) effect of the CO_2/H_2 ratio, (b) effect of the total concentration of CO_2 and H_2, (c) effect of the reaction temperature, and (d) effect of the reaction time. Reaction conditions: catalyst 50 mg, 300 W Xe lamp full irradiation and (a) $(CO_2 + H_2)/N_2$ 40%/60%, 200 °C, 3 h; (b) CO_2/H_2 1/3, 200 °C, 3 h; (c) $CO_2/H_2/N_2$ 10%/30%/60%, 3 h; and (d) $CO_2/H_2/N_2$ 10%/30%/60%, 200 °C, spades (/) photothermal conditions, clubs (♣) thermal conditions, and diamonds (◆) photocatalytic conditions respectively.

the photothermal reaction). However, their combination is beneficial for the CO_2 reduction, indicating that the excellent catalytic performances stemmed from their synergistic promotion effect.

As mentioned above, the present catalytic system could achieve the photothermal CO_2 reduction to C_{2+} hydrocarbons, but only needs to enhance the concentrations of CO_2 and H_2 to 25% and 75%. Fig. S9† shows the catalytic performances of the reaction. Under the conditions of 200 °C and 3 h, the highest C_{2+} selectivity and activity reached 30.8% and 7.5 mmol g_{cat}^{-1} h^{-1} obtained after 3 h of reaction.

The results indicated that the multifunctional applications of the trimetallic Co–Cu–Mn catalysts derive from not only the multicomponents of the catalysts, but also the interaction effects between the components.

Photoelectric properties of the Co–Cu–Mn catalysts

The study of the catalytic performances confirmed that Co_3O_4 and Mn_2O_3 oxides are very important for the reaction, and this differs from the fully reduced Co-based catalysts in H_2 such as Co/CoO_x[29] and Co_6/MnO_x[5] catalysts in CO_2 thermal hydrogenation. This diversification is probably because photothermal catalysis needs more light-sensitive components such as Co_3O_4 and Mn_2O_3 due to their semiconductor nature,[52,53] while the thermal catalyst favours low-valent metals such as Co^0.

To further investigate the light-sensitive properties of the Co–Cu–Mn trimetallic catalysts, the UV-vis DRS spectra were investigated, and the results are shown in Fig. S10a.† The unreduced catalysts including $Co_7Mn_1O_x$, $Co_7Cu_1O_x$, and $Co_7Cu_1Mn_1O_x$ showed higher absorption than the corresponding reduced catalysts throughout the UV-vis region. This was because the former mainly contain Co_3O_4, which has strong absorption of d–d transitions.[54] Upon reduction, the Co_3O_4 amount decreased, leading to the decrease of absorption accordingly. As for the $Co_7Cu_1Mn_1O_x$(200, 300, 400, and 500) catalysts, with the increase of the reduction temperature, the absorption strength decreased gradually for the deep reduction of Co_3O_4 to CoO and Co^0 species. Both the $Co_7Cu_1O_x$(200) and $Co_7Cu_1Mn_1O_x$(500) catalysts showed a lower absorbance than the other samples because they did not contain the Co_3O_4 species, which was confirmed by the XRD tests.

The band gap energies (E_g) for the tested catalysts were calculated using the Kubelka–Munk (K–M) model.[55] The $Co_7Cu_1Mn_1O_x$(200) catalyst had a lower E_g value (1.86 eV) than those of the catalysts reduced at higher temperatures (Fig. S10b†). The $Co_7Cu_1Mn_1O_x$(500) catalyst, however, had the highest E_g (3.26 eV) value and showed a very low activity in the reaction. The low E_g value of the $Co_7Cu_1Mn_1O_x$(200) catalyst led to the feature that the electrons in the semiconductor could be easily excited under light irradiation. The lower band gap is conducive to visible light excitation, which was confirmed by the control experiments using different types of light including full irradiation (300–1100 nm), UV (300–420 nm), and visible light (420–800 nm). The catalytic performances obtained under visible light illumination are almost similar to those under UV-vis and full irradiation, as shown in Table S5.†

The photocurrent–time curves of the $Co_7Cu_1Mn_1O_x$(100, 200, 300, and 400) catalysts are shown in Fig. S10c.† All of these catalysts showed obvious photocurrent response behavior, indicating that they could be excited to generate electron–hole pairs.

Co_3O_4, Mn_2O_3, Cu_2O, and CoO are p-type semiconductors; however, after reduction, oxygen vacancies were created and regulated the p-type to a n-type semiconductor, which is confirmed by the Mott–Schottky curves shown in Fig. S10d.† All the catalysts showed dipolar (p-type and n-type) semiconductor properties, resulting from the multiple interfaces of the complex trimetallic catalyst.

The EIS Nyquist plots of the tested samples including $Co_7Cu_1Mn_1O_x$(100, 200, 300, and 500) showed similar arc radii, revealing that they have similar impedance values and electron transfer rates (Fig. S10e†).[56]

The photothermal effect was investigated *via* testing the stable temperature of the samples under vacuum (Fig. S11†). Under similar conditions, the catalyst temperatures were monitored using an infrared camera. Among the tested catalysts, the MnO_x catalyst showed the highest temperature (104.6 °C) under the full irradiation, while the CuO_x catalyst offered the lowest (88.3 °C). The $Co_7Cu_1Mn_1O_x$(200) catalyst showed a higher temperature (102.2 °C) than that of the $Co_7Cu_1Mn_1O_x$(500) (95.8 °C), indicating that the $Co_7Cu_1Mn_1O_x$(200) catalyst could provide a higher local heating environment. The results revealed that the presence of Mn could provide a higher local temperature for the catalyst.

In summary, the results obtained due to the photoelectrical characteristics indicated that the $Co_7Cu_1Mn_1O_x$(200) catalyst is a p-type and n-type semiconductor, showing a low band gap. All of these properties are closely related to the excellent catalytic activity in photothermal CO_2 reduction. However, it should be noted that the unique catalytic performances of the $Co_7Cu_1Mn_1O_x$(200) catalyst were derived from the synergistic effect of the adsorption effect, light-response properties, and photothermal effect.

Light effect and the proposed mechanism for photothermal CO_2 reduction

In the present catalytic system, the synergistic effect between light and heat had a great influence on the catalytic activity. Under light irradiation, the electrons of the $Co_7Cu_1Mn_1O_x$(200) catalyst could be excited to generate the electron–hole pairs. Generally, in photocatalysis, the excited electrons and holes can participate in reactions.[57] However, under photothermal conditions, the E_g value of the semiconductor is normally found to be lower, and the excited electrons recombine more easily with the photogenerated holes than under the traditional photocatalysis without heating.

To investigate the effects of the generated electron–hole pairs, we carried out two control experiments by adding sacrificial electron donors including *p*-xylene (~2.18 V *vs.* $Ag/AgCl_{sat}$) and anisole (1.92 V *vs.* $Ag/AgCl_{sat}$) in the absence of H_2.[18,25] As shown in Fig. S12,† both the reactions gave a very low CH_4

yield despite the fact that *p*-xylene and anisole could quench the photogenerated holes more efficiently than H_2. These results indicated that photocatalysis plays a minor role in the present photothermal CO_2 reduction. In this aspect, similar to the Ru-,[18] Rh-,[58] Au-,[58] and Ag-based[59] catalysts, the charge separation and recombination under light irradiation resulted in a local thermal effect at the surface of the catalyst, offering more energy to promote CO_2 reduction.

The mechanism for the photothermal CO_2 reduction to hydrocarbons is still unclear, and two reaction routes are generally accepted.[60] The first involves a CO intermediate, in which CO_2 is initially converted to CO, and CO could be further hydrogenated to hydrocarbons.[61] The other route is the direct CO_2 conversion. In this route, CO_2 is hydrogenated to carbonate, formate, and methoxy intermediates, and then hydrogenated to hydrocarbons. In this work, the CO formation activity was very low. To study the reaction pathway, we conducted the control experiments of replacing CO_2 by CO under the conditions given in Table 1, entry 8. Interestingly, the activities of CH_4 and C_{2+} were 4.9 and 7.3 mmol g_{cat}^{-1} h^{-1}, and their selectivities were 40.2% and 59.8%, respectively (Table 1, entry 8, Fig. S13, S14 *vs.* Table S6, entry 2, Fig. S15†). To exclude that the high CO concentration may occupy the active sites on the catalyst surface, a mixed gas of 2%CO/8%CO_2 (total 10%) was also reacted (Table S6, entry 3 and Fig. S16†). However, the activities of CH_4 and C_{2+} were 7.2 and 2.8 mmol g_{cat}^{-1} h^{-1} with the selectivities of 72.0% and 28.0%, respectively. The results implied that the presence of CO could not improve but reduce the CH_4 activity, meaning that in the photothermal CO_2 reduction, CH_4 is probably not formed *via* the CO intermediate route. However, CO was found to be beneficial for the C_{2+} synthesis, revealing that it is probably an intermediate for the formation of the C_{2+} hydrocarbon product.

The characterization results confirmed that the trimetallic $Co_7Cu_1Mn_1O_x(200)$ catalyst contains CoO, Co_3O_4, Cu_2O, Mn_2O_3, *etc*. During the reaction, the CoO species could be reduced to Co^0, which was recognized as the active site. The CoO and Cu_2O species could be reduced by H_2 to Co^0 and Cu^0 during the reaction, which was confirmed by the XPS results (Fig. 5). In the present photothermal CO_2 hydrogenation, metal oxides such as Co_3O_4 and Mn_2O_3 were very important for the reaction because they are semiconductors, which could generate electrons and holes under light illumination. A quick recombination of electrons and holes provides a local heating environment for the catalysts, and further promotes the reaction.[5] In addition, Mn_2O_3 could offer Lewis acidic sites to enhance CO_2 and H_2 adsorption capacity of the catalyst.

Cu species could promote the partial reduction of cobalt oxides to CoO and Co^0 and maintain the presence of CoO and Co_3O_4 prior to and during the reaction, and reduce the temperature of catalyst reduction. Besides, the CO_2-TPD tests and the control experiments confirmed that the Cu species or the Cu–Co interfaces could provide strong CO_2 adsorption sites to convert CO_2 to CO, and further form C_{2+} hydrocarbons.

It should be mentioned that, although CH_4 was probably not formed *via* the CO route, CO could be produced with an activity of 1.1 mmol g_{cat}^{-1} h^{-1} (entry 8, Table 1). Importantly, the higher concentration of CO could make it easily coupled into the C_{2+} products over the same $Co_7Cu_1Mn_1O_x(200)$ catalyst. Thus, C_{2+} hydrocarbons could be formed by increasing the CO_2 concentration.

In addition, the present protocol could be extended to photothermal CO hydrogenation. We conducted the reaction over the $Co_7Cu_1Mn_1O_x(200)$ catalyst under the similar conditions given in Table 1, entry 8, and the results are shown in Fig. S17.† The photothermal activity is about 7 times higher than that of the thermal activity, and the selectivity of the C_{2+} products is higher than that of CH_4, which is similar to CO_2 hydrogenation. The results indicated that the present trimetallic Co–Cu–Mn catalyst has multifunctional applications as shown in photothermal CO hydrogenation.

The reusability and stability studies of the $Co_7Cu_1Mn_1O_x(200)$ catalyst

The reusability of the $Co_7Cu_1Mn_1O_x(200)$ catalyst was investigated, and the results are shown in Fig. 8a. For comparison, the CO_2 reduction reactions were alternatively conducted under photothermal and thermal conditions. The results revealed that the present catalyst possesses good reusability in the reaction, and after using for 18 times, it still offered an activity of higher than 10 $mmol_{CH_4}$ g_{cat}^{-1} h^{-1}. Besides, the results also confirmed that the activities under photothermal conditions were much higher than those under thermal conditions. The used catalysts were characterized by XRD and XPS, and the results are shown in Fig. 5, respectively.

The activity loss is probably caused by catalyst agglomeration, which was confirmed by the TEM images of the catalyst after being used 18 times (Fig. S18).† The size of the used catalyst increased in the range 40–90 nm.

Fig. 8b shows the temporal stability of the $Co_7Cu_1Mn_1O_x(200)$ catalyst in a continuous flow operation (details are given in the ESI†). The catalyst offered approximately 20 mmol g_{cat}^{-1} h^{-1} of CH_4 after a short induction period of 3 h, and maintained higher than 18 mmol g_{cat}^{-1} h^{-1}

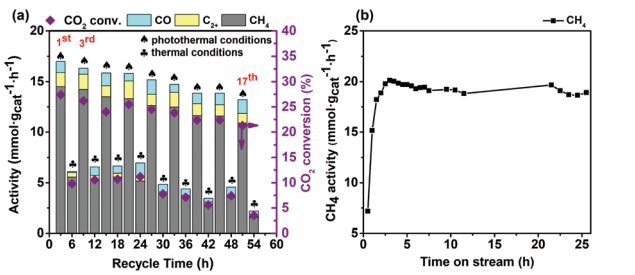

Fig. 8 Reusability (a) and temporal stability (b) studies of $Co_7Cu_1Mn_1O_x(200)$ in photothermal CO_2 reduction. Reaction conditions: (a) catalyst 50 mg, 200 °C, $CO_2/H_2/N_2$ 10%/30%/60%, full irradiation for photothermal conditions; (b) catalyst 50 mg, 200 °C, $CO_2/H_2/N_2$ 10%/30%/60% 20 mL min^{-1}, full irradiation.

even after 25 hours of reaction. The result showed that the present $Co_7Cu_1Mn_1O_x(200)$ catalyst has a long-term temporal stability, confirming that it has a potential industrial application.

Conclusions

In summary, a trimetallic Co–Cu–Mn catalytic system for photothermal CO_2 reduction was constructed by a simple co-precipitation method. The metal compositions and reduction temperatures of the catalysts affected their activities remarkably, and the screened $Co_7Cu_1Mn_1O_x(200)$ catalyst could offer 14.5 mmol g_{cat}^{-1} h^{-1} of CH_4 at low CO_2 (10%) and H_2 (30%) concentrations. Importantly, the catalyst system could produce C_{2+} hydrocarbons with an activity of 7.5 mmol g_{cat}^{-1} h^{-1} and a selectivity of 30.8% by only improving the CO_2 and H_2 concentrations to 25% and 75%, respectively. High activities stemmed from the multicomponents of the catalyst, especially the metallic Co^0, Cu^0, and CoO, Co_3O_4, Cu_2O, and Mn_2O_3 semiconductors. The Cu species could tune the reduction characteristics, and further tune the balance of Co^{2+} and Co^{3+}. The Mn species could enhance the CO_2 and H_2 adsorption, and also offer a high local temperature for the nanocatalyst. The present strategy of partial reduction of the Co–Cu–Mn trimetallic catalyst not only highlights the route for using solar energy to produce valuable chemicals under mild conditions especially low CO_2 concentration, but also constructs the highly efficient trimetallic catalysts with multifunctional applications in photothermal catalysis.

Conflicts of interest

There are no conflicts to declare.

Acknowledgements

The authors gratefully acknowledge the financial supports from the National Natural Science Foundation of China (21978160, 21776170, 22078182, 21706152, and 21908139), the Natural Science Basic Research Plan in Shaanxi Province of China (Program No. 2019JLM-16, 2019JQ-772, and 2019JQ-782) and the Key Industrial Innovation Project of Shaanxi Provincial Science and Technology Department (2019ZDLGY06-04).

Notes and references

1 M. He, Y. Sun and B. Han, *Angew. Chem., Int. Ed.*, 2013, **52**, 9620–9633.
2 L. Wang, Y. Dong, T. Yan, Z. Hu, A. A. Jelle, D. M. Meira, P. N. Duchesne, J. Y. Y. Qiu, E. E. Storey, Y. Xu, W. Sun, M. Ghoussoub, N. P. Kherani, A. S. Helmy and G. A. Ozin, *Nat. Commun.*, 2020, **11**, 2432.
3 B. Zhou, P. Ou, N. Pant, S. Cheng, S. Vanka, S. Chu, P. T. Rashid, G. Botton, J. Song and Z. Mi, *Proc. Natl. Acad. Sci. U. S. A.*, 2020, **117**, 1330–1338.
4 M. Cui, Q. Qian, J. Zhang, Y. Wang, B. B. A. Bediako, H. Liu and B. Han, *Chem*, 2021, **7**, 726–737.
5 Z. He, M. Cui, Q. Qian, J. Zhang, H. Liu and B. Han, *Proc. Natl. Acad. Sci. U. S. A.*, 2019, **116**, 1254–12659.
6 Z. Ma and M. D. Porosoff, *ACS Catal.*, 2019, **9**, 2639–2656.
7 R. De, S. Gonglach, S. Paul, M. Haas, S. S. Sreejith, P. Gerschel, U.-P. Apfel, T. H. Vuong, J. Rabeah, S. Roy and W. Schöfberger, *Angew. Chem., Int. Ed.*, 2020, **59**, 10527–10534.
8 Y. Wang, X. Shang, J. Shen, Z. Zhang, D. Wang, J. Lin, J. C. S. Wu, X. Fu, X. Wang and C. Li, *Nat. Commun.*, 2020, **11**, 3043.
9 A. Weihard, S. P. Argent and V. Sans, *Nat. Commun.*, 2021, **12**, 231.
10 Z. He, Q. Qian, J. Ma, Q. Meng, H. Zhou, J. Song, Z. Liu and B. Han, *Angew. Chem., Int. Ed.*, 2016, **55**, 737–741.
11 L. Wang, E. Guan, Y. Wang, L. Wang, Z. Gong, Y. Cui, X. Meng, B. C. Gates and F.-S. Xiao, *Nat. Commun.*, 2020, **11**, 1033.
12 M. Rahaman, K. Kiran, I. Z. Montiel, V. Grozovski, A. Dutta and P. Broekmann, *Green Chem.*, 2020, **22**, 6497–6509.
13 G. Chen, R. Gao, Y. Zhao, Z. Li, G. I. N. Waterhouse, R. Shi, J. Zhao, M. Zhang, L. Shang, G. Sheng, X. Zhang, X. Wen, L.-Z. Wu, C.-H. Tung and T. Zhang, *Adv. Mater.*, 2017, 1734663.
14 F. Sastre, A. V. Puga, L. Liu, A. Corma and H. García, *J. Am. Chem. Soc.*, 2014, **136**, 6798–6801.
15 J. Albero, E. Dominguez, A. Corma and H. Garcia, *Sustain. Energy Fuels*, 2017, **7**, 1303–1307.
16 F. Zhang, Y.-H. Li, M.-Y. Qi, Y. M. A. Yamada, M. Anpo, Z.-R. Tang and Y.-J. Xu, *Chem. Catal.*, 2021, **1**, 1–26.
17 P. G. O'Brien, A. Sandhel, T. E. Wood, A. A. Jelle, L. B. Hoch, D. D. Perovic, C. A. Mims and G. A. Ozin, *Adv. Sci.*, 2014, **1**, 1400001.
18 D. Mateo, J. Albero and H. García, *Joule*, 2019, **3**, 1–14.
19 A. A. Jelle, K. K. Ghuman, P. G. O'Brien, M. Hmadeh, A. Sandhel, D. D. Perovic, C. V. Singh, C. A. Mims and G. A. Ozin, *Adv. Energy Mater.*, 2018, **8**, 1702277.
20 J. Ren, S. Ouyang, H. Xu, X. Meng, T. Wang, D. Wang and J. Ye, *Adv. Energy Mater.*, 2016, 1601657.
21 X. Meng, T. Wang, L. Liu, S. Ouyang, P. Li, H. Hu, T. Kako, H. Iwai, A. Tanaka and J. Ye, *Angew. Chem., Int. Ed.*, 2014, **53**, 11478–11482.
22 C. Wang, S. Fang, S. Xie, Y. Zheng and Y. H. Hu, *J. Mater. Chem. A*, 2020, **8**, 7990–7394.
23 J. Jia, H. Wang, Z. Lu, P. G. O'Brien, M. Ghoussoub, P. Duchesne, Z. Zheng, P. Li, Q. Qiao, L. Wang, A. Gu, A. A. Jelle, Y. Dong, Q. Wang, K. K. Ghuman, T. Wood, C. Qian, Y. Shao, C. Qiu, M. Ye, Y. Zhu, Z.-H. Lu, P. Zhang, A. S. Helmy, C. V. Singh, N. P. Kherani, D. D. Perovic and G. A. Ozin, *Adv. Sci.*, 2017, 1700252.
24 M. Cabrero-Antonino, S. Remiro-Buenamañana, M. Souto, A. A. García-Valdivia, D. Choquesillo-Lazarte, S. Navalón, A. Rodríguez-Diéguez, G. M. Espallargas and H. García, *Chem. Commun.*, 2019, **55**, 10932–10935.

25 D. Mateo, J. Albero and H. García, *Energy Enviorn. Sci.*, 2017, **10**, 2392–2400.
26 M.-P. Jiang, K.-K. Huang, J.-H. Liu, D. Wang, Y. Wang, X. Wang, Z.-D. Li, X.-Y. Wang, Z.-B. Geng, X.-Y. Hou and S.-H. Feng, *Chem*, 2020, **6**, 2335–2346.
27 J. A. Rodriguez, P. Liu, D. J. Stacchiola, S. D. Senanayake, M. G. White and J. G. Chen, *ACS Catal.*, 2015, **5**, 6696–6706.
28 R. Lang, X. Du, Y. Huang, X. Jiang, Q. Zhang, Y. Guo, K. Liu, B. Qiao, A. Wang and T. Zhang, *Chem. Rev.*, 2020, **120**, 11986–12043.
29 K. Zhao, M. Calizzi, E. Moioli, M. Li, A. Borsay, L. Lombardo, R. Mutschler, W. Luo and A. Zuttel, *J. Energy Chem.*, 2021, **53**, 241–250.
30 M. Ao, G. H. Pham, V. Sage, V. Pareek and S. Liu, *Fuel Process. Technol.*, 2019, **193**, 141–148.
31 Y. Xiang, R. Barbosa, N. Kruse and X. Li, *ACS Catal.*, 2015, **5**, 2929–2934.
32 Y. Wang, S. Kattel, W. Gao, K. Li, P. Liu, J. G. Chen and H. Chen, *Nat. Commun.*, 2019, **10**, 1166.
33 A. A. S. Goncalves, P. B. Faustino, J. M. Assaf and M. Jaroniec, *ACS Appl. Mater. Interfaces*, 2017, **9**, 6079–6092.
34 Y. Li, H. S. Pillai, J. Lattimer, N. M. Adli, S. Karakalos, M. Chen, L. Guo, H. Xu, J. Yang, D. Su, H. Xin and G. Wu, *ACS Catal.*, 2020, **10**, 3945–3957.
35 M. Sharma, J.-H. Jang, D. Y. Shin, J. A. Kwon, D.-H. Lim, D. Choi, H. Sung, J. Jang, S.-Y. Lee, K. Y. Lee, H.-Y. Park, N. Jung and S. J. Yoo, *Energy Environ. Sci.*, 2019, **12**, 2200–2211.
36 L. Martin, H. Martinezz, D. Poinot, B. Pecquenard and F. L. Cras, *J. Phys. Chem. C*, 2013, **117**, 4421–4430.
37 Z. Geng, Y. Wang, J. Liu, G. Li, L. Li, K. Huang, L. Yuan and S. Feng, *ACS Appl. Mater. Interfaces*, 2016, **8**, 27825–27831.
38 L. Lukaskuk, N. Yigit, R. Rameshan, E. Kolar, D. Teschner, M. Havecker, A. Knop-Gericke, R. Schlogl, K. Fottinger and G. Rupprechter, *ACS Catal.*, 2018, **8**, 8630–8641.
39 J. Su, Z. Zhang, D. Fu, X. Xu, B. Shi, X. Wang, R. Si, Z. Jiang, J. Xu and Y. Han, *J. Catal.*, 2016, **336**, 94–106.
40 B. Rivas-Murias and V. Salgueiriño, *J. Raman Spectrosc.*, 2017, **48**, 837–841.
41 X. Jiang, X. Nie, X. Guo, C. Song and J. G. Chen, *Chem. Rev.*, 2020, **120**, 7984–8034.
42 Y. Xiang, V. Chitry, P. Liddicoat, P. Felfer, J. Cairney, S. Ringer and N. Kruse, *J. Am. Chem. Soc.*, 2013, **135**, 7114–7117.
43 Z.-H. He, C.-S. Jiang, K. Wang, Z.-Y. Wang, N. Li, W.-T. Wang and Z.-T. Liu, *Catal. Today*, 2020, **356**, 579–588.
44 M. Tahir, B. Tahir, N. A. S. Amin and A. Muhammad, *Energy Convers. Manag.*, 2016, **119**, 368–378.
45 Z.-H. He, N. Li, K. Wang, W.-T. Wang and Z.-T. Liu, *Mol. Catal.*, 2019, **470**, 120–126.
46 O. A. Bulavchenko, E. Y. Gerasimov and T. N. Afonasenko, *Dalton Trans.*, 2018, **47**, 17153–17159.
47 W. Yang, Y. Peng, Y. Wang, Y. Wang, H. Liu, Z. Su, W. Yang, J. Chen, W. Si and J. Li, *Appl. Catal., B*, 2020, **278**, 119279.
48 W. Yang, S. Wang, K. Li, S. Liu, L. Gan, Y. Peng and J. Li, *Chem. Eng. J.*, 2019, **364**, 448–451.
49 C.-I. Ahn, D.-W. Jeong, J. M. Cho, H.-S. Na, W.-J. Jang, H.-S. Roh, J.-H. Choi, S.-H. Um and J.-W. Bae, *Microporous Mesoporous Mater.*, 2016, **221**, 204–211.
50 O. A. Bulavchenko, E. Y. Gerasimov and T. N. Afonasenko, *Dalton Trans.*, 2018, **47**, 17153–17159.
51 G. Chen, R. Gao, Y. Zhao, Z. Li, G. I. N. Waterhouse, R. Shi, J. Zhao, M. Zhang, L. Shang, G. Sheng, X. Zhang, X. Wen, L. Wu, T. Tung and T. Zhang, *Adv. Mater.*, 2018, **30**, 1704663.
52 J. Zhao, Z. Zhao, N. Li, J. Nan, R. Yu and J. Du, *Chem. Eng. J.*, 2018, **353**, 805–813.
53 Y. Zeng, H. Li, Y. Xia, L. Wang, K. Yin, Y. Wei, X. Liu and S. Luo, *ACS Appl. Mater. Interfaces*, 2020, **12**, 44608–44616.
54 Z. Li, J. Liu, Y. Zhao, R. Shi, G. I. N. Waterhouse, Y. Wang, L.-Z. Wu, C.-H. Tung and T. Zhang, *Nano Energy*, 2019, **60**, 467–475.
55 A. Umasadharshini, M. Bououdina, M. Venkateshwarlu, C. Manoharan and P. Dhamodharan, *Surf. Interfaces*, 2020, **19**, 100535.
56 Q. Wan, J. Zhang, B. Zhang, D. Tan, L. Yao, L. Zheng, F. Zhang, L. Lin, X. Cheng and B. Han, *Green Chem.*, 2020, **22**, 2750–2754.
57 N. Li, M. Liu, B. Yang, W. Shu, Q. Shen, M. Liu and J. Zhou, *J. Phys. Chem. C*, 2017, **121**, 2923–2932.
58 X. Zhang, X. Li, D. Zhuang, N. Q. Su, W. Yang, H. O. Everitt and J. Liu, *Nat. Commun.*, 2017, **8**, 14542.
59 P. Christopher, H. Xin and S. Linic, *Nat. Chem.*, 2011, **3**, 467–472.
60 B. Miao, S. S. K. Ma, X. Wang, H. Su and S. H. Chan, *Catal. Sci. Technol.*, 2016, **6**, 4048–4058.
61 B. Tahir, M. Tahir and N. S. Amin, *Energy Convers. Manage.*, 2015, **90**, 272–281.